

# Correlation between mechanical strength of amorphous TiO<sub>2</sub> nanotubes and their solid state crystallization pathways

Zhonghui Gao,<sup>[a]</sup> Zhangxiang Hao,<sup>[f]</sup> Min Yi,<sup>[d]</sup> Ying Huang,<sup>[e]</sup> Yiming Xu,<sup>[b]</sup> Ying Zhao,<sup>[d]</sup> Zhaoyang Li,<sup>[b]</sup> Shengli Zhu,<sup>[b]</sup> Baixiang Xu,<sup>[d]</sup> Porun Liu,<sup>\*,[c]</sup> Feng Ryan Wang,<sup>\*,[f]</sup> Yunhui Huang,<sup>\*,[a]</sup> Huijun Zhao<sup>[c]</sup> and Xianjin Yang<sup>[b]</sup>

**Abstract:** Developing TiO<sub>2</sub> crystals with specific morphologies and nanostructured architectures is highly desirable in energy storage, conversion and catalysis. Thermally activated amorphous-to-crystal transition provides effective growth of poly or monocrystalline TiO<sub>2</sub>, while the understanding of different crystallization pathways at the solid state is still a challenge. Herein, we report a successful correlation between mechanical strength of the TiO<sub>2</sub> precursors and their different crystallization pathways. Well-defined anatase TiO<sub>2</sub> single nanocrystals or anatase polycrystalline nanotubes are obtained via rapid heating of two amorphous TiO<sub>2</sub> precursors. Those two precursors have similar morphology and do not show any difference in SEM, XRD, XPS and Raman analysis while nanoindentation indicates that single TiO<sub>2</sub> crystals are formed from the precursor with less mechanical strength. This correlation will help optimize the precursor synthesis and predict the crystallization pathways in the solid state precursor. Thus well-defined nanocrystals with controlled morphology will be achieved. Such single TiO<sub>2</sub> crystals show higher storage capacity of Na<sup>+</sup> than that of

polycrystalline ones in sodium ion batteries.

## Introduction

The control of crystal growth at nanometer scale is of key importance for achieving desired materials properties. To this end, a number of approaches, such as wet chemical, vapor deposition and thermal activated solid-state growth methods, have been developed to thermodynamically or kinetically control the crystal growth.<sup>[1-6]</sup> Surface capping agents are widely used in the liquid phase to achieve desired particle shapes.<sup>[7]</sup> In the gas phase, catalysts are used to structurally direct the growth of materials at the vapor-catalyst interface.<sup>[8]</sup> In comparison, nanocrystal synthesis via solid state crystallization of precursor materials is less understood and lack of effective control. Unlike the molecular precursors in the liquid and gas phase synthesis, the precursors here are composite, amorphous or poor crystalline solids that are pre-synthesized via sol-gel, electrochemical, and co-precipitation methods.<sup>[9-11]</sup> Those precursors usually have ill-defined structures<sup>[12,13]</sup> that are difficult to analyze via conventional chemical characterization methods such as X-ray diffraction (XRD), X-ray photoelectron spectroscopy (XPS) and Raman spectroscopy. Here we introduce nanoindentation as the mechanical characterization technique to probe the overall mechanical strength of the precursor materials. The results are then correlated to the crystallization performance of the precursors, suggesting a new way to predict and optimize solid state synthesis of nanomaterials.

TiO<sub>2</sub> anatase crystals are chosen to be the target materials due to their wide applications in photovoltaic, photocatalytic water splitting, photonic and optoelectronic devices and electrochemical energy storage.<sup>[14]</sup> Recently, they are suggested to be an attractive anode material for Na-ion battery.<sup>[15]</sup> The interaction between Na<sup>+</sup> and TiO<sub>2</sub> nanocrystals is shape dependent and plays a huge role in the Na<sup>+</sup> intercalation. Two amorphous TiO<sub>2</sub> nanotubes are synthesized via electrochemical deposition under different potentials. Those two nanotubes have similar morphology and do not show any difference in scanning transmission microscopy (SEM), XRD, XPS and Raman analysis. Nanoindentation is then introduced and shows that nanotubes formed at higher voltages have lower mechanical strength, suggesting a smaller particle domain inside the tubes. Single TiO<sub>2</sub> crystals (s-crystal) are then formed from such precursor while polycrystalline TiO<sub>2</sub> nanotubes (p-tube) are obtained from precursor with higher mechanical strength.

The Na ion battery equipped with s-crystal anodes demonstrates higher rate and longer cyclability than those with

- [a] Dr. Z.H. Gao, Prof. Yunhui Huang  
School of Materials Science and Engineering,  
Tongji University  
Shanghai 201804, P. R. China  
E-mail: huangyh@tongji.edu.cn
- [b] Mr. Y. M. Xu, Prof. Z. Y. Li, Prof. S. L. Zhu, Prof. X. J. Yang  
School of Materials Science and Engineering,  
Tianjin University  
Tianjin 300350, P. R. China
- [c] Dr. P. R. Liu, Prof. H. J. Zhao  
Centre for Clean Environment and Energy,  
Griffith School of Environment Gold Coast Campus, Griffith  
University  
Queensland 4222, Australia  
E-mail: p.liu@griffith.edu.au
- [d] Dr. M. Yi, Dr. Y. Zhao, Prof. B. X. Xu  
Institute of Materials Science  
Technische Universität Darmstadt  
Darmstadt 64287, Germany
- [e] Dr. Y. Huang  
School of Materials Science and Engineering,  
Yunana Key Laboratory for Micro/Nano Materials & Technology,  
Yunnan University  
Kunming, Yunnan 650091, P. R. China
- [f] Dr. Z. X. Hao, Dr. F. R. Wang  
Department of Chemical Engineering,  
University College London  
Torrington Place, London, WC1E 7JE, United Kingdom  
Email: ryan.wang@ucl.ac.uk

Supporting information for this article is given via a link at the end of the document.

p-tube anodes, due to the presence of more exposed {001} facets at s-crystal.

## Results and Discussion

TiO<sub>2</sub> nanotubes with controlled sizes are prepared via electrochemical deposition over Ti substrate at anodization voltages of 40 V and 60 V. The obtained tubes are monodispersed, ordered and well orientated. The hole diameter, bottom diameter and length of the tubes are  $120 \pm 7.5$  nm,  $122 \pm 4$  nm and  $9.5 \pm 1$   $\mu$ m for 40 V TiO<sub>2</sub>, and  $165.8 \pm 8$  nm,  $176.2 \pm 11$  nm and  $18.5 \pm 2$   $\mu$ m for 60 V TiO<sub>2</sub>, respectively (Figure 1a,d and Figure S1, Supporting Information). As a result, the average numbers of tubes per 1  $\mu$ m<sup>2</sup> are 94 to 56.8. A rapid thermal annealing at 450 °C is applied to both tubes for 2 min, forming p-tube from 40 V TiO<sub>2</sub> and s-crystal from 60 V TiO<sub>2</sub> (Figure 1b,c,e,f.). Selected area electron diffraction (SAED) confirms polycrystallinity and monocrystallinity of the p-tube and s-crystal, respectively. P-tubes retain the tubular shape of the original precursor, while S-crystals are in quasi-decahedral shapes around the size of  $170 \pm 31$  nm. According to the crystallographic symmetries of anatase TiO<sub>2</sub> single nanocrystals, the flat surfaces at both ends are (001) facets (Figure 1e).

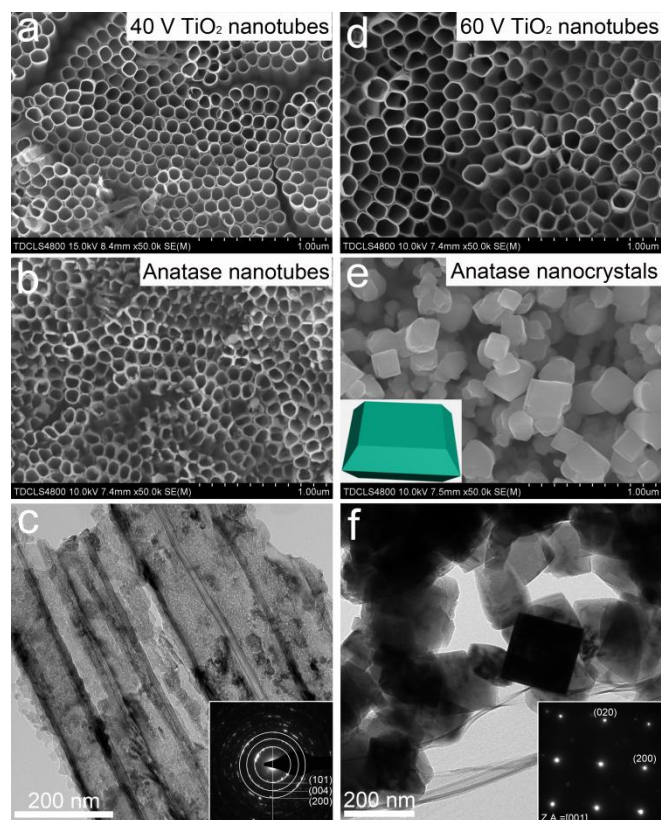


**Figure 1.** The amorphous-to-crystalline transitions of TiO<sub>2</sub> nanotubes formed at 40 V and 60 V. (a,d) SEM image of TiO<sub>2</sub> nanotubes anodized at 40 V (a) and 60 V (d). (b,c) SEM (b) and transmission electron microscopy (TEM) (c) images of p-tubes. (e,f) SEM (e) and TEM (f) images of s-crystals. The insets in (e) and (f) are corresponded SAED patterns.

The formation of p-tubes and s-crystals are monitored by taking SEM images at different annealing stages. No obvious morphology change is observed for 40 V TiO<sub>2</sub> nanotubes (Figure

2a). This then leads to the formation of p-tubes. In comparison, polyhedral nanocrystals are found with 60 V TiO<sub>2</sub> nanotubes within 30 s thermal treatment (Figure 5b). As the reaction time extended to 50 s, all the TiO<sub>2</sub> nanotubes have been converted into s-crystals.

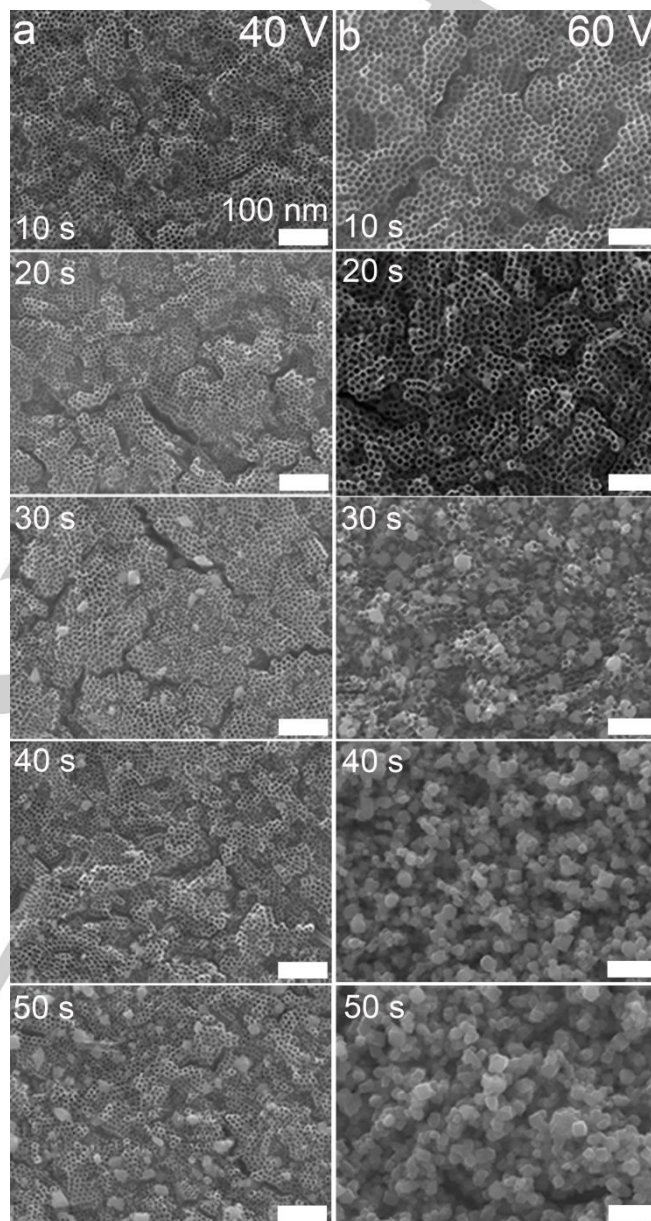


**Figure 2.** SEM images obtained by rapid heating of 40 V (a) and 60 V (b) TiO<sub>2</sub> nanotubes for 10 s and 20, 30, 40, and 50 s at 450 °C. All scale bars are 100 nm.

All diffraction peaks of the TiO<sub>2</sub> precursors show only the characteristics of  $\alpha$ -Ti substrate while that of the p-tubes and s-crystals are indexed to the crystalline anatase TiO<sub>2</sub> (space group *I41/amd*, Figure 3a). The characteristic peaks for p-tubes and s-crystals are identified as 25.3° (101), 37.8° (004), 48° (200), 53.9° (105), 55.1° (211), and 62.7° (204). The peak intensities of s-crystals are higher than those of p-tubes, suggesting higher crystallinity of the former. Diffraction peaks of the  $\alpha$ -Ti substrate can be found on the p-tube samples, indicating the weak diffraction of x-ray from the p-tubes. This further confirms their

pore crystallinity. Typical Raman scattering finger prints are also found for p-tubes and s-crystals (Figure 3b). The  $400\text{ cm}^{-1}$ ,  $520\text{ cm}^{-1}$  and  $640\text{ cm}^{-1}$  scatterings correspond to the  $B_{1g}$ ,  $A_{1g}$ ,  $E_{1g}$  vibration modes, respectively. Those scatterings are absent for the  $\text{TiO}_2$  precursors, further confirming their amorphous nature.

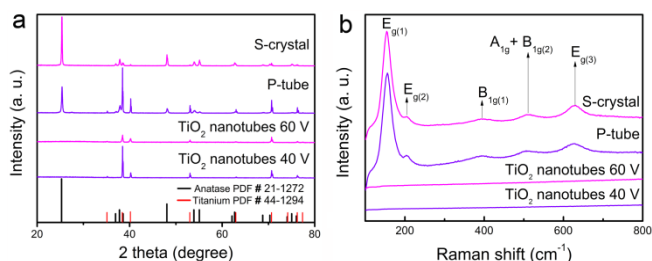


**Figure 3.** (a) XRD patterns of p-tubes, s-crystals and  $\text{TiO}_2$  precursor. (b) Corresponded Raman spectra.

XPS is used to probe the surface chemical composition of both precursors and nanocrystals. In general, there are no visible difference among the two precursors, the p-tubes and the s-crystals (Figure 4). Titanium (Ti 2p), oxygen (O 1s) and fluorine (F 1s) are found at the  $\text{TiO}_2$  surface. The photoemission at 458.9 eV and 464.7 eV are typical transition for Ti 2p (3/2) and Ti 2p (1/2), suggesting the presence of  $\text{Ti}^{4+}$  (Figure 4a,d). Deconvolution of the O peaks is performed via a curve fitting procedure using Gaussian/Lorentzian product functions.<sup>[16]</sup> Ti-O (530.3 eV), Ti-OH (531.5 eV) and  $(\text{CH}_2\text{OH})_2$  (531.5 eV) signals are identified (Figure 4b,e).<sup>[17]</sup> The fluorine component at 684.6 eV is assigned to  $\text{TiF}_6^{2-}$  (Figure 4c,f).<sup>[18]</sup> F comes from the  $\text{NH}_4\text{F}$ , which is used to etch the surface  $\text{TiO}_2$  film into tubes while  $(\text{CH}_2\text{OH})_2$  is used to control the speed of  $\text{F}^-$  etching.

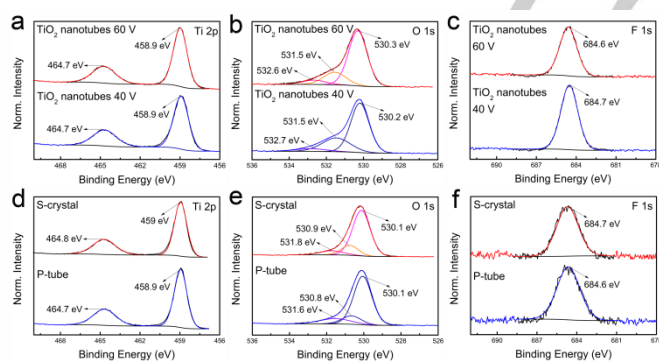


**Figure 4.** (a-c) XPS at Ti 2p, O 1s, and F 1s regions for two amorphous precursors. (d-f) XPS at Ti 2p, O 1s, and F 1s regions for n-tubes and s-crystals. The red and blue solid lines in b and e are the raw data of the XPS, and the colored lines in them represent the fitted lines.

The SEM, XRD, Raman and XPS studies do not reveal any obvious difference between the two  $\text{TiO}_2$  precursors that are synthesized at 40 V and 60 V. However, they do behave differently during crystallization, forming p-tubes and s-crystals that are distinct from each other. We hypothesize that this is due to the difference in the microscopic structures between the amorphous precursors, which is difficult to characterize. Such difference in microscopic structures can be possibly reflected by the mechanical properties of the materials. We therefore introduce the nanoindentation technique that is widely applied in

the characterization of mechanical strength in thin film coatings. Such technique presses the thin film with a very precisely shaped tip as an indenter, and measures the load of the force  $P$  as a function of volume that is changed (Displacement  $h$ ). Hardness ( $H$ ) of the materials can then be calculated.

Here, the measurement takes place in the longitudinal direction of the  $\text{TiO}_2$  nanotube precursors (40 V and 60 V) (Figure S2a,b, supporting information). The morphology of two precursors obtained at the maximum load  $P_{\text{max}} = 1000\text{ }\mu\text{N}$  with a  $8\text{ }\mu\text{m}$  tip indenter are very similar (Figure S2c,d), indicating the same route deformation of the nanotubes. The indenter tip is in contact with all the tubes within its cross section. The tube walls are broken by the tips and collapsed into particles that partially clogged the rest of the tubes. The fracture of the tube was localized at the contact region of the tip indenter and does not expand to the surrounding tubes. There was no pile-up behavior. The tube walls are broken by the tips and collapsed into particles that partially clogged the rest of the tubes.

Figure 5 shows the loading-unloading curves for both  $\text{TiO}_2$  precursors at  $P_{\text{max}} = 80, 300, 1000,$  and  $3000\text{ }\mu\text{N}$ . The sharp slopes of the unloading curves show the no elastic deformation and the brittleness of  $\text{TiO}_2$  tubes.<sup>[19-21]</sup> For both  $\text{TiO}_2$  tubes,  $h$  significantly increases in the early stage of loading up to  $1000\text{ }\mu\text{N}$ . No obvious difference between the two  $\text{TiO}_2$  tubes is found at low  $P_{\text{max}}$ . When the  $P_{\text{max}}$  is increased to  $3000\text{ }\mu\text{N}$ , the  $\text{TiO}_2$  tubes that are formed at 60 V give a larger displacement  $h$  of  $800\text{ nm}$  than that formed at 40 V. This larger displacement is reproducible, as indicated in Figure 5c where the average of 10 measurements is given.

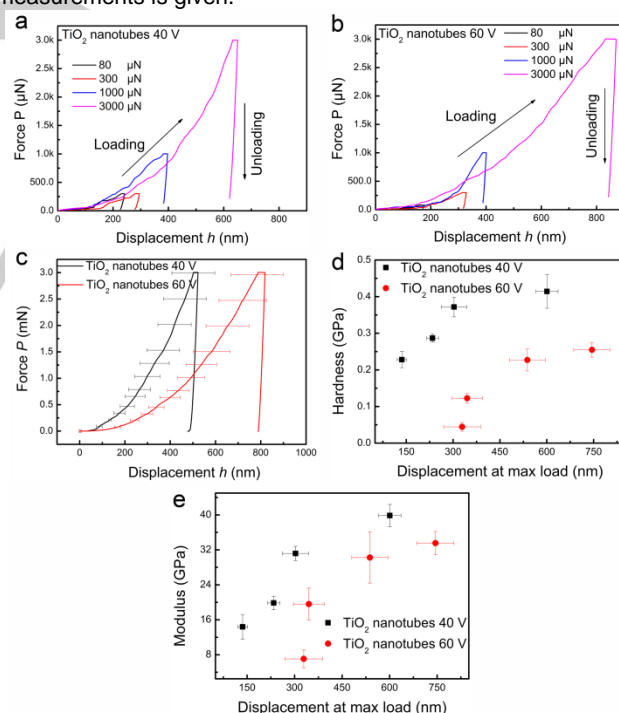


**Figure 5.** (a,b) Force–displacement responses of the 40 V (a) and 60 V (b)  $\text{TiO}_2$  nanotubes. (c) The average force–displacement responses at  $3000\text{ }\mu\text{N}$  of 10 measurements for both samples. (d-e) The hardness (d), Young's modulus (e).

The nanotube hardness increases as the displacement under maximum load ( $h_{\text{max}}$ ) is increased for both 40 V and 60 V  $\text{TiO}_2$  nanotubes (Figure 5d). This is due to the filling of the holes by the new cracked  $\text{TiO}_2$  particles which then increases the

overall mechanical strength of the tubes. The higher hardness of 40 V TiO<sub>2</sub> nanotubes than that of the 60 V ones at different displacements is due to the fast filling of small holes (120 ± 7.5 nm for 40 V TiO<sub>2</sub> and 165.8 ± 8 nm for 60 V ones) in the former. The similar phenomenon at different sizes of holes is also found for the Young's modulus (Figure 5e).

We further use a reported fracture model to calculate the apparent fracture stress of TiO<sub>2</sub> nanotubes.<sup>[22-24]</sup> The calculation is based on the assumption that: (1) The radial direction of the nanotubes is neglected due to the small thickness of tube wall; (2) the loss of fragmented TiO<sub>2</sub> species to the surround is not considered; (3) the mechanical interaction within the nanotubes themselves are also negligible. The apparent fracture stress of the TiO<sub>2</sub> nanotube can be then calculated as:<sup>[22]</sup>

$$\sigma_a = \frac{F}{A_d} = \frac{\pi d^2 \tan \theta \delta_f \sigma_c}{A_d} = \frac{\pi d^2 \tan \theta \delta_f \sigma_c L}{A_d L} \equiv C \varepsilon_a \quad (1)$$

Where,  $2\theta$  is the angle between the inner and outer walls,  $\delta_f$  is the fracture displacement,  $\sigma_c$  is the compressive strength,  $A_d$  is the force per unit area,  $L$  is the length of the tube,  $\varepsilon_a = \delta_f/L$  is defined as the apparent fracture strain. The  $C$  value reveals the apparent stress-strain relationship in the longitudinal direction of the nanotubes. A higher  $C$  value 0.14 is obtained for 60 V TiO<sub>2</sub> nanotubes than that of 40 V ( $C$  value 0.08), indicates the accelerated the densification of broken species for the 60 V TiO<sub>2</sub> tubes.

The overall mechanical study indeed shows that the mechanical strength (in the forms of hardness and Young's modulus) of 40 V TiO<sub>2</sub> nanotubes is higher than that of 60 V TiO<sub>2</sub> nanotubes. This is so far the only difference in the materials property between those two amorphous precursors. We then correlate this with the crystallization behaviors of those precursors under thermal treatment. Thus, s-crystals are formed from the TiO<sub>2</sub> precursors with weak mechanical strength. The use of mechanical measurement is then serves as the indication of particle crystallization behaviors.

We further evaluation the Na<sup>+</sup> storage capacity of p-tubes and s-crystals as anode materials in Na ion batteries. In the first cathodic scan during cyclic voltammetry (CV), the current beginning at 0.55 V is attributed to formation of the solid electrolyte interface (SEI). For both samples, the pair of redox peaks locate at approximately 0.65 V (cathodic) and 0.8 V (anodic) (Figure 6a,b), corresponding to the discharge and charge process.<sup>[25-27]</sup> High rate measurement is the key challenge for rechargeable Na-ion batteries due to the difficulty in insertion and extraction of the large Na ions (1.02 Å) into the host structure of TiO<sub>2</sub>, which inevitably cause an irreversible damage to its crystal structure. For the s-crystals, the discharge capacity reaches approximate 215 mAh g<sup>-1</sup> at the 50 mAh g<sup>-1</sup>, and decreases to 157, 100, 57, 44, and 24 mAh g<sup>-1</sup> at the rates of 100, 200, 400, 600, and 800 mAh g<sup>-1</sup>, respectively (Figure 6c). The p-tubes give slightly higher capacity of 220 mAh g<sup>-1</sup> at 50 mAh g<sup>-1</sup>, while the capacity become slightly lower to 160, 101, 51, 33, and 11 mAh g<sup>-1</sup> at the rate of 100, 200, 400, 600, and 800 mAh g<sup>-1</sup>, respectively. When the rate is reset to 50 mAh g<sup>-1</sup> after various rates, the discharge capacity of s-crystals (163 mAh g<sup>-1</sup>) becomes higher than that of n-tubes (146 mAh g<sup>-1</sup>). This indicates that s-crystal is more stable than p-tubes at high-rate cycling. The s-crystals also show a better long-term cycling performance than that of n-tube, especially after 90th cycle (Figure 6d). The coulombic efficiencies of both of s-crystal and

p-tube systems become higher than 90% after 13 cycles. In summary, these results suggest that a better high-rate and long-term cyclability performances are obtained by using s-crystals as the anode materials than that of the p-tubes.

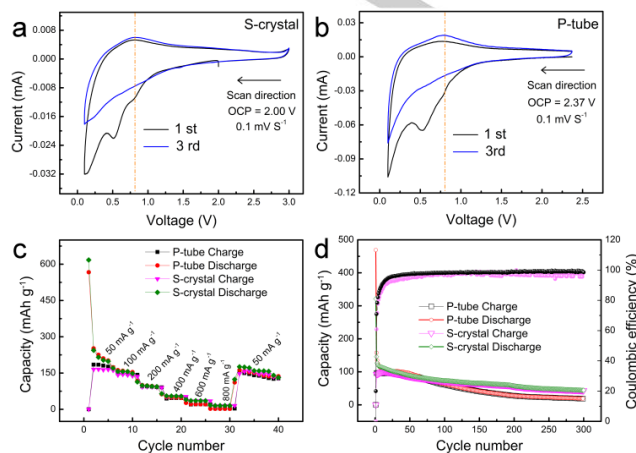


**Figure 6.** Electrochemical performances of the TiO<sub>2</sub> s-crystal and p-tubes. (a,b) CV curves of s-crystal (a) and p-tubes (b) at a scan rate of 0.1 mV S<sup>-1</sup>. (c) Cycle performance of both materials at various charge and discharge rates. (d) Cyclic performance and Coulombic efficiency of both materials in Na-ion half cells at a current density of 500 mAh g<sup>-1</sup>.

The better rate performance of s-crystal is due to the more exposed (001) facets, which have the high reactivity with Na ions in the electrolyte. Density function theory (DFT) simulation shows that the required energy to adsorbed Na<sup>+</sup> on (001) surface is lower than that of (101) surface (Figure 7 and Table 1).<sup>[28]</sup> Surface F<sup>-</sup> is considered due to observation of fluorine via XPS. For anatase TiO<sub>2</sub> (101) surface, the adsorption energy of Na<sup>+</sup> onto hollow and top site is 4.89 and 4.85 eV, respectively. They are higher than the energy at (001) surface, which are 2.94 and 2.35 eV, respectively. The same trend is also observed with F free surface (Figure S3 and Table S1, supporting information). Those results show a strong facet dependent Na<sup>+</sup> adsorption.

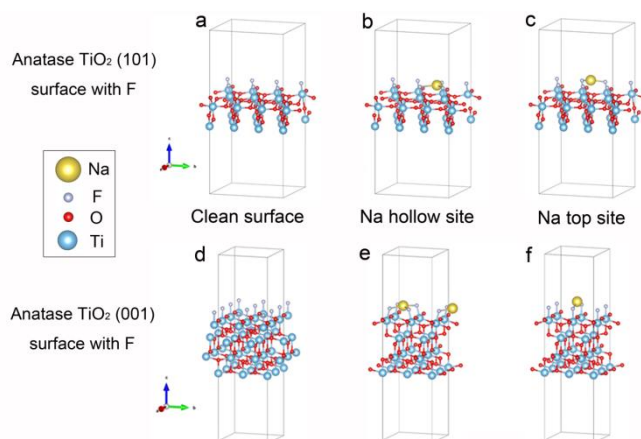


**Figure 7.** Adsorption energies of Na<sup>+</sup> on the (101) and (001) surfaces of anatase TiO<sub>2</sub> via DFT simulations. (a) TiO<sub>2</sub> (101) surface (1 × 3 × 1 unit cell). (b-c) Na<sup>+</sup> adsorption on hollow and top site of TiO<sub>2</sub> (101) surface. (d) TiO<sub>2</sub> (001) surface (2 × 2 × 1 unit cell). (e-f) Na<sup>+</sup> adsorption on hollow and top site of TiO<sub>2</sub> (001) surface.

Table 1 Adsorption energy of Na<sup>+</sup>

Anatase TiO <sub>2</sub> surface	Adsorption site	$nS E_{ad}$ (eV)
(001) surface with F <sup>-</sup>	hollow site	2.9372
	top site	2.3489
(101) surface with F <sup>-</sup>	hollow site	4.896
	top site	4.845

## Conclusions

We have successfully demonstrated the correlation between materials mechanical strength and their solid phase crystallization pathways. The materials with weak mechanical strength will lead to fast crystallization upon thermal treatment, forming high crystalline products. Here the formation of TiO<sub>2</sub> single nanocrystal and polycrystalline tubes are verified by this correlation. The use of mechanical characterization in the crystallization field will help probe and optimize materials crystallization pathways, achieving well defined products for in energy storage, conversion and catalysis applications.

## Experimental Section

**Preparation of anatase TiO<sub>2</sub> materials.** All chemicals were used as received. Ammonium fluoride (NH<sub>4</sub>F), ethylene glycol, and anhydrous ethanol were purchased from Tianjin Chemical Reagent Factory (China). The surfaces of 1 mm thick titanium (Ti) (99.9% purity) substrates were mechanically polished using 600 #, 1000 #, and 1500 # abrasive papers, rinsed for 10 min in an ultrasonic bath filled with ethanol, and then dried in air. After ultrasonic cleaning, the surfaces were anodized with a two-electrode cell with pure Ti foil as the working electrode and platinum foil as the counter electrode. The Ti foils were anodized at different direct current (DC) voltages applied by a DC power supply in an electrolyte solution containing ethylene glycol, H<sub>2</sub>O, and 0.5 wt % NH<sub>4</sub>F. The holding voltage was set as 40 V and 60 V, respectively. The holding time was 1 h for 40 V and 60 V. The electrolyte type and the temperature (25 °C) were maintained constant for all anodizing experiments. After anodization, the prepared samples were thoroughly rinsed with DI water and dried in air. The as-prepared amorphous TiO<sub>2</sub> nanotubes were annealed at 450 °C for 2 min to get the s-crystals and p-tubes without distinguishable morphology change. The rapid thermal treatment method in this study is studied in detail in our submitted manuscript.<sup>[29]</sup>

**Characterization of the mechanical strength of TiO<sub>2</sub> nanotube.** The mechanical properties of the anodized TiO<sub>2</sub> nanotubes were probed by nanoindentation. Nanoindentation experiments in the longitudinal direction of the nanotubes were conducted using a nanoindenter (Nano DMA II/III transducer). A flat tip indenter with a diameter of approximately 8 μm was used. Different stress states can be applied to the tip contact region. The inherent strength of the nanotubes is then evaluated. The applied force  $P$  was increased at a constant loading rate up to the maximum force  $P_{max}$  and then unloaded to zero at the same loading rate.

**Chemical characterizations.** Field-emission scanning electron microscopy (FE-SEM S4800, Hitachi, Japan) and transmission electron microscopy (TEM TecnaiG2F20, Philips, the Netherlands) were used to observe the morphology of the TiO<sub>2</sub> materials. The SEM and TEM measurements were obtained at an acceleration voltage of 10 kV and 200 kV, respectively. X-Ray diffraction (XRD) patterns were obtained on a conventional powder diffractometer (Rigaku DMAX 2500, Japan) using Cu K $\alpha$  irradiation at a scan rate ( $2\theta$ ) of 0.02° s<sup>-1</sup> to determine the structures of the obtained samples. Raman spectra were acquired with a Renishaw 100 system Raman spectrometer using 632.8 nm He-Ne laser. The XPS data was detected by using a Kratos Analytical Axis Ultra X-ray photoelectron spectrometer equipped with a monochromatic Al X-ray

source (Al K $\alpha$ , 1.487 keV). The C 1s was used as the charge reference with a binding energy of 284.8 eV.

**Electrochemical measurements.** The coin cell contains the working electrode, Na metal as the counter and reference electrode, glass fibre membrane (GF/D, Whatman) as the separator and 1 M NaClO<sub>4</sub> in a mixture of ethylene carbonate and propylene carbonate (2:1 by volume) as the electrolyte. Galvanostatic charge–discharge tests were carried out on a Neware battery measurement system at various current densities with a cutoff potential window of 0.05–3V at room temperature. CV measurements at various scan rates from 0.1 mV s<sup>-1</sup> were carried out on a CHI 660E potentiostat.

**Density-functional theory (DFT) modeling.** The adsorption energy of Na<sup>+</sup> on the one side of (001) and (101) surfaces of anatase was calculated in the slab model by using the computational code OpenMX,<sup>[30]</sup> which is based on optimized pseudopotentials and pseudo-atomic-orbital basis functions within DFT. The generalized gradient approximation (GGA) was employed with the exchange-correlation functional of Perdew-Burke-Ernzerhof (PBE). The cutoff energy was set to be 500 Ry. For the slab model, the (2×2) anatase (001) and (3×1) anatase (101) surfaces are used. Both the anatase surfaces with and without fluorine (F) coverage were considered. F atoms at the surface were set to directly interact with the 5-fold coordinated Ti (Ti<sub>5f</sub>) surface cations.<sup>[31]</sup> For relaxation of the slab model, 11×11×1  $k$ -point mesh was used in the full Brillouin zone. The convergence criteria for the maximum force on each atom and the total energy were 2×10<sup>-4</sup> Hartree/Bohr and 2×10<sup>-6</sup> Hartree, respectively. In the self-consistent calculations of the total energy, 17×17×1  $k$ -point mesh and energy convergence criteria of 10<sup>-6</sup> Hartree were used. The adsorption energy was calculated by

$$E_{ad} = (E^{TiO_2} + E^{Na} - E^{TiO_2+Na}) / (nS),$$

in which  $E^{TiO_2}$  is the energy of the anatase surfaces with or without F coverage,  $E^{Na}$  the energy of single Na<sup>+</sup>,  $E^{TiO_2+Na}$  the energy of surface covered by  $n$  Na<sup>+</sup> (here  $n=1$ ), and  $S$  the surface area.

## Acknowledgements

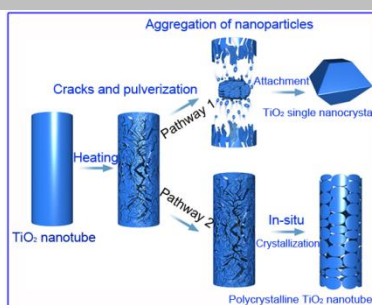
This work was financially supported by the Recruitment Program of Global Experts “1000 Talents Plan” of China (WQ20121200052), National Natural Science Foundation of China (51771131), the EPSRC First Grant project (EP/P02467X/1) and Royal Society research grant (RG160661).

**Keywords:** TiO<sub>2</sub> nanotubes • Nanoindentation • Mechanical strength • Na-ion battery

- [1] M. A. Lovette, A. R. Browning, D. W. Griffin, J. P. Sizemore, R. C. Snyder, M. F. Doherty, *Ind. Eng. Chem. Res.* **2008**, *47*, 9812–9833.
- [2] C. Z. Yuan, H. B. Wu, Y. Xie, X. W. Lou, *Angew. Chem. Int. Ed.* **2014**, *53*, 1488–1504
- [3] C. Xu, L. B. Wang, Z. B. Liu, L. Chen, J. K. Guo, N. Kang, X. L. Ma, H. M. Cheng, W. C. Ren, *Nat. Mater.* **2015**, *14*, 1135–1141.
- [4] I. Stassen, M. Styles, G. Greci, H. V. Gorp, W. Vanderlinden, S. De Feyter, P. Falcaro, D. De Vos, P. Vereecken, R. Ameloot, *Nat. Mater.* **2016**, *15*, 304–310.
- [5] S. P. Albu, A. Ghicov, S. Aldabergenova, P. Drechsel, D. LeClere, G. E. Thompson, J. M. Macak, P. Schmuki, *Adv. Mater.* **2008**, *20*, 4135–4139.
- [6] B. Xia, H. Z. Huang, Y. C. Xie, *Mater. Sci. Eng., B* **1999**, *57*, 150–154.
- [7] K. N. Olafson, R. Li, B. G. Alamani, J. D. Rimer, *Chem. Mater.* **2016**, *28*, 8453–8465.
- [8] X. Ling, Y. H. Lee, Y. X. Lin, W. J. Fang, L. L. Yu, M. S. Dresselhaus, J. Kong, *Nano Lett.* **2014**, *14*, 464–472.
- [9] H. Shin, H. S. Jung, K. S. Hong, J. K. Lee, *J. Solution Chem.* **2005**, *178*, 15–21.

- [10] Z. H. Gao, Z. D. Cui, S. L. Zhu, Y. Q. Liang, Z. Y. Li, X. J. Yang, *J. Nanopart. Res.* **2014**, *16*, 2191.
- [11] Z. L. Liu, L. Hong, B. Guo, *J. Power Sources* **2005**, *143*, 231–235.
- [12] J. C. Yu, J. G. Yu, W. K. Ho, Z. T. Jiang, L. Z. Zhang, *Chem. Mater.* **2002**, *14*, 3808–3816.
- [13] S. W. Liu, J. G. Yu, M. Jaroniec, *Chem. Mater.* **2011**, *23*, 4085–4093.
- [14] G. Liu, H. G. Yang, J. Pan, Y. Q. Yang, G. Q. Liu, H. M. Cheng, *Chem. Rev.* **2014**, *114*, 9559–9612.
- [15] H. B. Wu, J. S. Chen, H. H. Hng, X. W. Lou, *Nanoscale* **2012**, *4*, 2526–2542.
- [16] D. Gonbeau, C. Guimon, G. Pfister-Guillouzo, A. Levasseur, G. Meunier, R. Dormoy, *Surf. Sci.* **1991**, *254*, 81–89.
- [17] Y. Z. Huang, D. J. Blackwood, *Electrochim Acta* **2005**, *51*, 1099–1107.
- [18] D. Regonini, A. Jaroenworarluck, R. Stevensa, C. R. Bowena, *Surf. Interface Anal.* **2010**, *42*, 139–144.
- [19] M. Pang, D. F. Bahr, *J. Mater. Res.* **2001**, *16*, 2634–2643.
- [20] G. M. Pharr, W. C. Oliver, *MRS Bulletin* **1992**, *17*, 28–33.
- [21] R. Saha, W. D. Nix, *Acta Mater.* **2002**, *50*, 23–38.
- [22] H. Hirakata, K. Ito, A. Yonezu, H. Tsuchiayi, S. Fujimoto, K. Minoshima, *Acta Mater.* **2010**, *58*, 4956–4967.
- [23] F. S. Stein, S. Thiemann, S. Berger, R. Hahn, P. Schmuki, *Acta Mater.* **2010**, *58*, 6317–6323.
- [24] O. K. Varghese, *J. Mater. Res.* **2003**, *18*, 156–165.
- [25] H. G. Yang, C. H. Sun, S. Z. Qiao, J. Zou, G. Liu, S. C. Smith, H. M. Cheng, G. Q. Lu, *Nature* **2008**, *453*, 638–641.
- [26] Z. H. Bi, M. P. Paranthaman, P. A. Menchhofer, R. R. Dehoff, C. A. Bridges, M. F. Chi, B. K. Guo, X. G. Sun, S. Dai, *J. Power Sources* **2013**, *222*, 461–466.
- [27] C. J. Chen, Y. W. Wen, X. L. Hu, X. L. Ji, M. Y. Yan, L. Q. Mai, P. Hu, B. Shan, Y. H. Huang, *Nat. Commun* **2015**, *6*, 6929.
- [28] K. T. Kim, G. Ali, K. Y. Chung, C. S. Yoon, H. Yashiro, Y. K. Sun, J. Lu, K. Amine, S. T. Myung, *Nano Lett.* **2014**, *14*, 416–422.
- [29] Z. H. Gao, Y. Zhao, H. F. Wang, Y. Wang, Y. M. Xu, B. X. Xu, L. R. Zheng, C. H. Jin, P. Liu, H. G. Yang, H. J. Zhao, X. J. Yang, Y. H. Huang, *Nature communications*, NCOMMS-18-14461, *under review*.
- [30] T. Ozaki, *Phys. Rev. B* **2003**, *67*, 155108.
- [31] O. Lamiel-Garcia, S. Tosoni, F. Illas, *J. Phys. Chem. C* **2014**, *118*, 13667–13673.

Correlation between mechanical strength of the  $\text{TiO}_2$  precursors with their different crystallization pathways and their structural properties, e.g., the high-rate and long-term cyclability in sodium ion batteries.



Zhonghui Gao,<sup>[a]</sup> Zhangxiang Hao,<sup>[f]</sup> Min Yi,<sup>[d]</sup> Ying Huang,<sup>[e]</sup> Yiming Xu,<sup>[b]</sup> Ying Zhao,<sup>[d]</sup> Zhaoyang Li,<sup>[b]</sup> Shengli Zhu,<sup>[b]</sup> Baixiang Xu,<sup>[d]</sup> Porun Liu,<sup>\* [c]</sup> Feng Ryan Wang,<sup>\* [f]</sup> Yunhui Huang,<sup>\* [a]</sup> Huijun Zhao<sup>[c]</sup> and Xianjin Yang<sup>[b]</sup>

**Page No. 1 – Page No. 7**  
**Correlation between mechanical strength of amorphous  $\text{TiO}_2$  nanotubes and their solid state crystallization pathways**